




Article

The Shape of the Chameleon Fifth-Force on the Mass Components of Galaxy Clusters

Lorenzo Pizzuti ^{1,*}, Valentina Amatori ², Alexandre M. Pombo ³ and Sandeep Haridasu ^{4,5,6}

¹ Dipartimento di Fisica G. Occhialini, Università degli Studi di Milano Bicocca, Piazza della Scienza 3, 20126 Milano, Italy

² Department of Physics, ETH Zurich, Otto-Stern-Weg 1, 8093 Zurich, Switzerland; vamatatori@student.ethz.ch

³ Central European Institute for Cosmology and Fundamental Physics (CEICO), Institute of Physics of the Czech Academy of Sciences, Na Slovance 2, 182 21 Praha, Czech Republic; pombo@fzu.cz

⁴ SISSA, Via Bonomea 265, 34136 Trieste, Italy; sharidas@sisssa.it

⁵ Institute for Fundamental Physics of the Universe (IFPU), Via Beirut 2, 34014 Trieste, Italy

⁶ INFN-Sezione di Trieste, Via Valerio 2, 34127 Trieste, Italy

* Correspondence: lorenzo.pizzuti@unimib.it

Abstract: In the context of chameleon gravity, we present a semi-analytical solution of the chameleon field profile in an accurately modelled galaxy cluster's mass components, namely the stellar mass of the Brightest Cluster Galaxy (BCG), the baryonic mass in galaxies other than the BCG, the mass of the Intra-Cluster Medium (ICM) and the diffuse cold dark matter (CDM). The obtained semi-analytic profile is validated against the numerical solution of the chameleon field equation and implemented in the MG-MAMPOST code for kinematic analyses of galaxy clusters in modified gravity scenarios. By means of mock halos, simulated both in GR and in modified gravity, we show that the combination of the velocities and positions of cluster member galaxies, along with the data of the stellar velocity dispersion profile of the BCG, can impose constraints on the parameter space of the chameleon model; for a cluster generated in GR, these constraints are at the same level as a joint lensing+kinematics analysis of a cluster modelled with a single mass profile, without the BCG data.

Keywords: modified gravity; galaxy clusters; cosmology



Citation: Pizzuti, L.; Amatori, V.; Pombo, A.M.; Haridasu, S. The Shape of the Chameleon Fifth-Force on the Mass Components of Galaxy Clusters. *Universe* **2024**, *10*, 443. <https://doi.org/10.3390/universe10120443>

Academic Editors: Jaime Haro Cases and Supriya Pan

Received: 31 October 2024

Revised: 25 November 2024

Accepted: 28 November 2024

Published: 30 November 2024



Copyright: © 2024 by the authors. Licensee MDPI, Basel, Switzerland. This article is an open access article distributed under the terms and conditions of the Creative Commons Attribution (CC BY) license (<https://creativecommons.org/licenses/by/4.0/>).

1. Introduction

The discovery of the late-time accelerated expansion of the Universe [1,2] presented one of the most formidable mysteries in modern physics. In order to explain the observed acceleration, the cosmological constant [3,4], Λ , was incorporated into General Relativity (GR), forming the foundation of the current framework of cosmological research: the standard Λ CDM model [5].

Supported by a broad array of observations [6,7], the Λ CDM model is widely regarded as the best descriptor of the observed Universe's expansion history. Nonetheless, despite its successes, the cosmological constant on which the model is based still lacks a fundamental explanation within the framework of standard physics [8].

In pursuit of a physical motivation for the cosmological constant, several alternatives have been proposed over the past decades. Of particular interest are models that modify GR—the foundation of the Standard Cosmological model—at large scales [9,10] by introducing an additional scalar field (scalar-tensor theories [11,12]) that is capable of replicating the cosmological constant's effect [13]. The introduction of this scalar field adds a component to the gravitational force [14,15], leaving measurable signatures on the formation and evolution of cosmic structures [16,17].

At the small-scale, high-density—when compared with the background density—Solar System scale, GR's precise validation [18] requires any Modified Gravity (MG) model to contain a screening mechanism in order to reconcile it with the well-established GR

measurements [19] at small scales while still impacting the dynamics at large, low-density, cosmological scales.

While several scalar-tensor models have been ruled out by gravitational waves observations (see e.g., [20,21]) or highly constrained by observations (e.g., [22–26]), their relative simplicity and rich phenomenology make them widely studied in different environments. One particularly interesting class of scalar-tensor theories that is viable at cosmological scales is the chameleon model [27]. In this framework, gravity’s effects vary with the environment due to a coupling between the additional scalar field (chameleon field) and matter. As a result, in the presence of a non-trivial scalar field, matter “feels” an additional fifth force, changing the formation and evolution of structures in the Universe.

In turn, the coupling feedback causes the scalar field to depend on the local energy density, leading to a very large field mass in high-density regions (suppressing the interaction) while containing a small, non-zero mass in low-density regions. The modulation of the scalar field by the environment results in a built-in screening mechanism where the fifth force is suppressed at small scales (recovering GR) while impacting large-scale dynamics.

In chameleon gravity models, the scalar field is characterized by the coupling constant (Q), which determines its interaction with matter, and the asymptotic value of the field at infinity (ϕ_∞). Both parameters have been strongly constrained by high-accuracy observational data across the laboratory (e.g., [15,28–30]), astrophysical (e.g., [31–33]), and cosmological scales (e.g., [34–37]).

Although the parameter space for viable chameleon theories is tightly constrained, it is nevertheless interesting to study their phenomenology at cluster scales, where some flexibility remains. Moreover, the peculiar screening mechanism provides an excellent model for exploring the possible effects of the fifth force on the mass components of clusters. For clusters, constraints are usually derived by modelling the total mass distribution of the cluster (baryonic and dark matter) using the Navarro–Frenk–White (NFW) profile [38]. However, recent studies have shown that some clusters favour an Isothermal or a Hernquist mass profile [39,40]. This preference for different mass models can have strong effects on the chameleon field profile—and the resulting fifth force.

In a previous work [41], we proposed studying the chameleon mechanism by means of a semi-analytical approximation of the chameleon field. This procedure allowed us to investigate the effect of the chameleon mechanism when changing the parametrization of the total cluster’s mass profile, showing how the efficiency of the screening—and, therefore, the constraints obtainable at the cluster’s scales—strongly depend on the assumed mass model. In this paper, instead of considering a single mass profile to describe the entire cluster’s mass distribution, we extend the analysis performed in [41] by introducing a semi-analytical approximation of the chameleon field profile in an *explicitly decomposed galaxy cluster’s key mass components*: the stellar mass of the Brightest Cluster Galaxy (BCG), the baryonic mass in galaxies, the Intra-Cluster Medium (ICM), and the diffuse, cold dark matter (CDM) component.

The semi-analytical approximation, based on the method proposed in [42], offers a straightforward and computationally efficient (when compared with a full numerical computation) strategy for studying the screening mechanism. Furthermore, it serves as a valuable tool for exploring the relationship between the parameters of the mass profiles and the chameleon field, emphasizing the key physical aspects of the screening mechanism. To ensure the validity of our semi-analytical approach, we compare it with a full numerical solution and confirm that it accurately reproduces the behaviour of the fifth force, with a maximum relative difference of 10^{-2} .

The validated semi-analytical solution is then fed into MG-MAMPOSSt code for kinematic analyses of galaxy clusters in modified gravity frameworks. Using mock galaxy cluster halos simulated in both GR and chameleon gravity, we demonstrate that combining the velocity and positional data of cluster member galaxies with the stellar velocity dispersion profile of the BCG strongly constrains the chameleon model’s parameter space.

The paper is structured as follows: Section 2 provides an overview of the fundamental theory of chameleon gravity and the screening mechanism. In Section 3, the semi-analytical expressions of the chameleon field and its gradient are obtained, assuming a four-component model for a cluster matter distribution; Section 4 further compares and validates the semi-analytical approach with the full numerical solutions of the (spherical) field equation.

2. Chameleon Gravity and Field Profile

The Lagrangian of a chameleon (real) scalar field [43], ϕ , conformally coupled with the matter fields $\psi^{(i)}$ can be written as

$$\mathcal{L} = \sqrt{-g} \left[-\frac{M_{\text{Pl}} R}{2} + \frac{(\partial\phi)^2}{2} + V(\phi) \right] + L_m(\psi^{(i)}, g_{\mu\nu}^{(i)}), \tag{1}$$

where $g_{\mu\nu}^{(i)}$ is the metric in the Jordan frame and g its determinant. The metric in the Einstein frame is recovered through a conformal transformation $g_{\mu\nu}^{(i)} = e^{-\frac{2Q_i\phi}{c^2 M_{\text{Pl}}}} \tilde{g}_{\mu\nu}$, with Q_i representing the coupling of the chameleon field to each matter field, $\psi^{(i)}$. As in, e.g., [34,44], in the following, a single coupling constant Q^1 for all matter components—dark and baryonic—will be assumed.² $M_{\text{Pl}} = 1/\sqrt{8\pi G}$ is the reduced Planck mass, and c is the speed of light. Non-relativistic matter has an energy density $\tilde{\rho} = \rho e^{\frac{Q\phi}{c^2 M_{\text{Pl}}}}$.

The potential $V(\phi)$ is a monotonic function of the scalar field, typically modelled as an inverse power-law:

$$V(\phi) = \lambda^{4+n} \phi^{-n}, \tag{2}$$

with $n \in \mathbb{N}$ and λ represents an energy scale that can be set to the dark energy scale [37].

The scalar (chameleon) field equation resulting from the Euler–Lagrange equations of Equation (1) in the quasi-static limit is

$$\nabla^2 \phi = V'(\phi) + \frac{Q}{M_{\text{Pl}} c^2} \sum_j \rho_j e^{\frac{Q\phi}{M_{\text{Pl}} c^2}}, \tag{3}$$

where a prime denotes differentiation with respect to the scalar field, and the index j covers all involved non-relativistic matter species. It is worth mentioning that ϕ/M_{Pl} has the dimension of energy per unit mass, i.e., it plays the role of an additional gravitational potential. On the right-hand side of Equation (3), one can notice that the dynamics of ϕ are dictated by an effective potential $V_{\text{eff}}(\phi)$ that encapsulates both the potential $V(\phi)$ and the matter–interaction feedback:

$$V_{\text{eff}}(\phi) \equiv V(\phi) + \sum_j \rho_j e^{\frac{Q\phi}{M_{\text{Pl}} c^2}}. \tag{4}$$

Current constraints on chameleon gravity [33,40,47] limit the field background to $\ll 1$ (in units of c^2). Thus, one can assume $Q\phi/(c^2 M_{\text{Pl}}) \ll 1$, and the effective potential can be approximated by $V_{\text{eff}}(\phi) \simeq V(\phi) + \rho_j (1 + Q\phi/(c^2 M_{\text{Pl}}))$. The resulting equation of motion is,

$$\nabla^2 \phi = \frac{Q}{c^2 M_{\text{Pl}}} \sum_j \rho_j + V'(\phi). \tag{5}$$

The profile of the chameleon field and the resulting fifth force is obtained by solving Equation (5) with suitable boundary conditions once a model is chosen for the matter density distribution. In the following, we employ a semi-analytical approach to reconstruct the field profile [34,41,42]. This consists of dividing the space–time into two regions: deep within the massive source, characterized by a field profile ϕ_{int} , and towards the low-density

outskirts, where the field is described by ϕ_{out} . The semi-analytic solution is then established by linking the interior with the exterior solution.

Deep inside the matter distribution, over-density region, the scalar field is suppressed and stays at the minimum of the effective potential, $\nabla^2\phi \approx 0$, effectively screening the fifth force. From Equation (5), the resulting scalar field inside the matter distribution is as follows:

$$\phi_{int} \approx \left(Q \frac{\rho_{tot}}{n\lambda^{4+n}M_{Pl}} \right)^{-\frac{1}{(n+1)}}, \tag{6}$$

where the total mass distribution is defined as $\rho_{tot} = \sum_j \rho_j$. On the other hand, the outer solution is obtained when the contribution of the scalar field potential, the first term on the right-hand side of Equation (5), is less dominant than the matter density and $\nabla^2\phi$. This describes the case where the chameleon field mediates a long-range fifth force, the matter density is still large compared to the background, and the scalar field has not settled to the minimum of the effective potential. The equation of motion for the exterior chameleon field is thus given by

$$\nabla^2\phi_{out} \approx Q \frac{\rho_{tot}}{M_{Pl}}. \tag{7}$$

In the following, let us assume a spherically symmetric matter distribution, $\rho_{tot} \equiv \rho_{tot}(r)$, which is a valid assumption for galaxy clusters in dynamical equilibrium [48,49]; the effect of triaxiality of halos in the chameleon mechanism is investigated in [37]. For spherically symmetric matter distributions, Equation (7) simplifies to

$$\frac{1}{r^2} \frac{d}{dr} \left(r^2 \frac{d\phi_{out}}{dr} \right) = Q \frac{\rho_{tot}(r)}{M_{Pl}}. \tag{8}$$

A single integration provides the following:

$$\frac{d\phi_{out}}{dr} r^2 = \frac{Q}{M_{Pl}} \int r^2 \rho_{tot}(r) dr + C, \tag{9}$$

with C as an integration constant. Notably, this expression shows that the fifth force in the outer region is proportional to the total mass profile given by the integral on the right-hand side of Equation (9). The Poisson equation for the gravitational potential in this region can now be written as follows:

$$\frac{d\Phi}{dr} = \frac{GM(r)}{r^2} + \frac{Q}{M_{Pl}} \frac{d\phi}{dr}, \tag{10}$$

where the second term expresses the contribution of the fifth force generated by the coupling between the chameleon field and the matter distribution. Equation (10) can be expressed in a Newtonian-like fashion by defining an *effective mass*

$$M_{eff} = \frac{Q}{G} \frac{r^2}{M_{Pl}} \frac{d\phi}{dr}, \tag{11}$$

from which the total dynamical mass can be derived:

$$M_{dyn} = M_{GR} + M_{eff}. \tag{12}$$

Note that, due to the null geodesic’s invariance under conformal transformations, the structure of the chameleon model produces lensing measurements that are only sensitive to the Newtonian part of the gravitational interaction; that is, the first term in Equation (10) [50]. This means that lensing surveys can be used as a complementary probe for the prior of the mass profile.

The scalar field can now be obtained as follows:

$$\phi_{out} = \frac{Q}{M_{Pl}} \int \frac{1}{r^2} \left[\int (r')^2 \rho_{tot}(r') dr' + C_s \right] dr. \tag{13}$$

The integration constant C_s can then be determined by imposing the continuity of ϕ_{int} and ϕ_{out} and their derivatives at the matching screening radius $r = S$, which denotes the transition scale between the two regimes. The term “screening radius” is used since, within a distance S , the effects of modified gravity are negligible, while at distances greater than S , the fifth force becomes significant. In the inner core of the halo, the field is significantly suppressed compared to its ambient value, $\phi_s \ll \phi_\infty$, making the interior solution negligible in comparison: $\phi_{\text{int}} \approx 0$.

3. Multi-Component Chameleon Solution

As previously stated, in a galaxy cluster, the matter distribution, ρ_j , can be generally modelled as the sum of four main components (see, e.g., [51,52]): the Brightest Cluster Galaxy (BCG), ρ_{BCG} , which dominates the mass profile and the dynamics in the innermost region ($r \lesssim 0.05$ Mpc); the hot Intra-Cluster Medium (ICM), ρ_{ICM} ; the mass density associated with the baryonic mass in galaxies (other than the BCG), ρ_* ; and the diffuse dark matter component (CDM), ρ_{CDM} . If a cluster is dynamically relaxed, all the mass distributions should be in equilibrium with the total gravitational potential and exhibit a nearly spherical disposition.

The total mass density, ρ_{tot} , is then

$$\rho_{\text{tot}}(r) = \rho_{\text{BCG}}(r) + \rho_{\text{ICM}}(r) + \rho_*(r) + \rho_{\text{CDM}}(r), \tag{14}$$

with each component modelled by the appropriate mass model. The BCG is, typically, a giant elliptical galaxy located close to the centre of the cluster’s gravitational potential. The associated surface brightness distribution is described by the de Vaucouleurs profile (e.g., [49,51]). The de-projection of this profile can be approximated as a Jaffe profile [53], which exhibits a simple analytical form, and thus will be used as a mass density model for the stellar distribution of the BCG using the following equation [54]:

$$\rho_{\text{BCG}}(r) = \frac{\rho_b}{\left(\frac{r}{r_J}\right)^2 \left(1 + \frac{r}{r_J}\right)^2}, \tag{15}$$

with the characteristic density written in terms of the total stellar mass, M_* , as

$$\rho_b = \frac{M_*}{4\pi r_J^3}; \tag{16}$$

In this way, the integral within a spherical volume of radius r reads

$$M(r) = M_* \frac{r}{r_J} \left(1 + \frac{r}{r_J}\right)^{-1}.$$

For the baryonic mass in galaxies, the profile is modelled by an NFW mass density profile, which was found to provide an adequate fit for the distribution of galaxies in clusters (e.g., [55,56]),

$$\rho_*(r) = \frac{\rho_*}{\frac{r}{r_*} \left(1 + \frac{r}{r_*}\right)^2}. \tag{17}$$

The hot intra-cluster gas of the ICM is modelled assuming an Isothermal β -profile [39,57]:

$$\rho_{\text{ICM}}(r) = \frac{\rho_g}{\left[\left(\frac{r}{r_g}\right)^2 + 1\right]^{3\alpha/2}}, \tag{18}$$

where we set $\alpha = 1$ in order to guarantee the convergence of the chameleon field profile with the background value at large radii (see [41]). Observe that, while other profiles were shown to better describe the ICM distribution in clusters (e.g., [58,59]), the relative

simplicity of the Isothermal ansatz makes it a widely used model distribution for the ICM (e.g., [52,60]).

Finally, for the diffuse dark matter distribution, a generalized NFW (gNFW hereafter) is assumed

$$\rho_{\text{CDM}}(r) = \frac{\rho_s}{\left(\frac{r}{r_s}\right)^\gamma \left(1 + \frac{r}{r_s}\right)^{3-\gamma}}, \tag{19}$$

where the inner slope is controlled by the additional real exponent $0 < \gamma < 2$.³ Note that in the MG-MAMPOSST analysis that will be presented in Section 5, the parameter r_{200} will be used instead of r_g . This is the radius of a sphere enclosing an over-density 200 times the critical density of the universe at a given redshift, $\rho_c(z) = 3H^2(z)/(8\pi G)$. The corresponding mass is $M_{200}^{(\text{CDM})} = 100 H^2(z)(r_{200})^3/G$.

The characteristic density of the gNFW model can now be obtained from r_{200} , r_s and γ as follows:

$$\rho_s = \left(\frac{r_{200}}{r_s}\right)^{\gamma-3} \frac{M_{200}^{(\text{CDM})}(3-\gamma)}{4\pi r_s^3 {}_2F_1\left(3-\gamma, 3-\gamma; 4-\gamma; -\frac{r_{200}}{r_s}\right)},$$

where ${}_2F_1(a, b, c, z)$ is the ordinary hypergeometric function.

The solution of Equation (8), assuming the expression of the density Equation (14), provides the expression for the gradient of the field:

$$\frac{d}{dr}\phi(r) = \begin{cases} \sim 0 & \text{if } r < S, \\ \frac{d\phi_{\text{out}}}{dr} & \text{if } r > S, \end{cases} \tag{20}$$

where

$$\begin{aligned} \frac{d\phi_{\text{out}}}{dr} = & \frac{C_s}{r^2} + \frac{Q}{M_{\text{Pl}}r^2} \left\{ \frac{\rho_s r^{3-\gamma} r_s^\gamma {}_2F_1\left(3-\gamma, 3-\gamma; 4-\gamma; -\frac{r}{r_s}\right)}{3-\gamma} - \frac{\rho_b r_J^4}{r+r_J} \right. \\ & \left. + \left[\rho_g r_g^3 \left(-\frac{r}{\sqrt{r^2+r_g^2}} - \log\left(\sqrt{r^2+r_g^2}-r\right) \right) + \rho_* r_*^3 \left(\frac{r_*}{r+r_*} + \log(r+r_*) \right) \right] \right\}. \end{aligned} \tag{21}$$

By integrating Equation (21), one can obtain the exterior field profile ($r > S$)

$$\begin{aligned} \phi(r) = & -\frac{C_s}{M_{\text{Pl}}r} + \frac{Q}{M_{\text{Pl}}r} \left[-\frac{(-1)^\gamma \rho_s r_s^3 \left(-\frac{r}{r_s}\right)^{3-\gamma} {}_2F_1\left(3-\gamma, 3-\gamma; 4-\gamma; -\frac{r}{r_s}\right)}{3-\gamma} \right. \\ & \left. - \rho_g r_g^3 \log\left(\sqrt{r^2+r_g^2}-r\right) + \rho_b r r_J^2 \log\left(\frac{r+r_J}{r}\right) + \rho_* r_*^3 \log(r+r_*) \right] \\ & + \frac{Q}{M_{\text{Pl}}r} \left(\frac{\rho_s r_s^2 r^{3-\gamma} (r+r_s)^{\gamma-2}}{\gamma-2} - \rho_b r_J^3 + \rho_* r_*^3 \right) + \frac{Q \rho_s r_s^2}{(\gamma-2)M_{\text{Pl}}} + \phi_\infty. \end{aligned} \tag{22}$$

The matching conditions at the screening radius, $\phi(S) = 0$, $\phi'(S) = 0$, provide the expression for the integration constant,

$$\begin{aligned} C_s = & \frac{Q}{M_{\text{Pl}}} \left\{ \frac{(-1)^\gamma \rho_s r_s^3 \left(-\frac{S}{r_s}\right)^{3-\gamma} {}_2F_1\left(3-\gamma, 3-\gamma; 4-\gamma; -\frac{S}{r_s}\right)}{3-\gamma} + \frac{\rho_b r_J^4}{S+r_J} \right. \\ & \left. + \rho_g r_g^3 \left(\frac{S}{\sqrt{S^2+r_g^2}} + \log\left(\sqrt{S^2+r_g^2}-S\right) \right) - \rho_* r_*^3 \left(\frac{r_*}{S+r_*} + \log(S+r_*) \right) \right\}, \end{aligned} \tag{23}$$

with the screening radius S given as the (real) numerical root of a “screening function”:

$$f_s(S) \equiv \frac{Q}{M_{\text{Pl}}} \left\{ -\frac{\rho_g r_g^3}{\sqrt{S^2 + r_g^2}} + \frac{\rho_b r_J^3}{S + r_J} + \frac{\rho_s r_s^2}{\gamma - 2} \left(1 - \left(\frac{S}{S + r_s} \right)^{2-\gamma} \right) - \frac{\rho_* r_*^3}{S + r_*} + \rho_b r_J^2 \log \left(\frac{S}{S + r_J} \right) \right\} + \phi_\infty = 0. \quad (24)$$

Note that f_s is a monotonically increasing function in S ; this implies that if $f_s > 0$ for $S \rightarrow 0$, then the cluster is unscreened. In Figure 1, the behaviour of the screening functions for a typical galaxy cluster is shown, varying the chameleon parameters (solid lines) and the gas and dark matter central densities (purple and red dashed lines, respectively). The intersection with the x-axis (denoted as a black solid horizontal line) provides the value of the screening radius S .

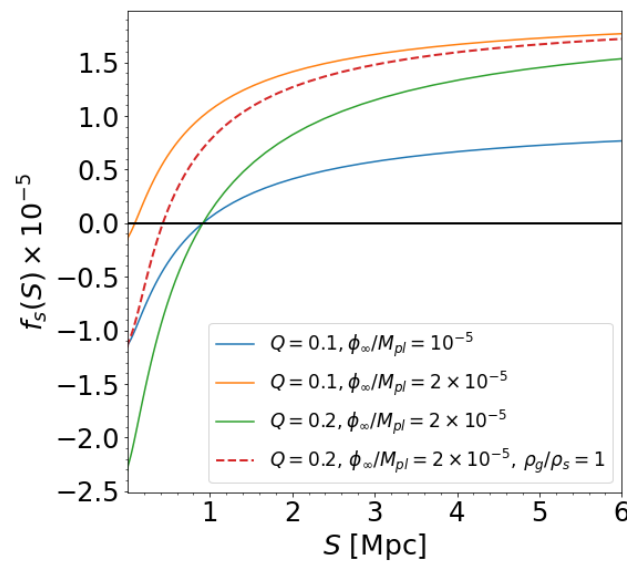


Figure 1. Solid lines: screening function $f_s(S)$ of Equation (24) for different values of the coupling and the value of the field at infinity (given in units of c^2). The density parameters are $\rho_s = 10^{15} \text{ M}_\odot/\text{Mpc}^3$; $r_s = 0.5 \text{ Mpc}$; $\gamma = 0.5$; $\rho_* = 10^{13} \text{ M}_\odot/\text{Mpc}^3$; $r_* = 0.3 \text{ Mpc}$; $\rho_g = 10^{14} \text{ M}_\odot/\text{Mpc}^3$; $r_g = 0.3 \text{ Mpc}$; $\rho_b = 10^{15} \text{ M}_\odot/\text{Mpc}^3$; $r_J = 0.03 \text{ Mpc}$. Red dashed line: setting $\rho_s \equiv \rho_g = 5 \times 10^{14} \text{ M}_\odot/\text{Mpc}^3$.

3.1. Comparison with a Single NFW Profile

Before further analysis, it is worth comparing the new multi-component modelling of the chameleon field with the results obtained when a single NFW profile was used to model the total cluster mass. For a reliable comparison, let us consider an NFW model characterized by the same value of $r_{200}^{(\text{tot})} = 2.15 \text{ Mpc}^4$ and $r_{-2}^{(\text{tot})} = 0.80 \text{ Mpc}$, where the latter is the radius at which the logarithmic slope of the density profiles is equal to -2 . For the multi-component case $\rho_s = 3.97 \times 10^{14} \text{ M}_\odot/\text{Mpc}^3$, $r_s = 0.87 \text{ Mpc}$, $\gamma = 0.7$ for the dark matter density, and $\rho_b = 10^{15} \text{ M}_\odot/\text{Mpc}^3$, $r_J = 0.03 \text{ Mpc}$ for the BCG profile. These values roughly correspond to the best fit found in the analysis of [49], where a kinematic analysis of cluster member galaxies and stellar velocity dispersion profile (VDP) of the BCG was applied to the data of the massive relaxed galaxy cluster MACS 1206 at $z = 0.44$. This high-quality dataset, complemented by the lensing information and X-ray data of the hot ICM, will be used to constrain the chameleon parameters in an upcoming work.

For the galaxies and gas profiles, assume $\rho_* = 3.55 \times 10^{13} \text{ M}_\odot/\text{Mpc}^3$, $r_* = 0.36 \text{ Mpc}$, $\rho_g = 2.54 \times 10^{14} \text{ M}_\odot/\text{Mpc}^3$ and $r_g = 0.37 \text{ Mpc}$, respectively. These values were obtained by fitting the observed galaxies and gas mass profiles with Equations (17) and (18).⁵

In the top panel of Figure 2, the total dynamical mass profiles, Equation (12), for the multi-component case (blue) and the single NFW model (red) are shown. The respective relative difference $[M_{\text{dyn}}^{(\text{multic})} - M_{\text{dyn}}^{(\text{NFW})}] / M_{\text{dyn}}^{(\text{NFW})}$ is presented in the lower plots. On average, the two profiles exhibit a discrepancy $\sim 10\%$, which becomes larger at $r \lesssim 0.1$ Mpc (e.g., $\lesssim 0.05 r_{200}^{(\text{tot})}$), where the contribution of the BCG becomes relevant. The red dots in the lower plots represent the region where the difference becomes negative (i.e., the NFW model predicts a higher total mass with respect to the multi-component case). The impact of the fifth force can clearly be observed as a bump—at $r \sim 10$ Mpc on the left and at $r \sim 2$ Mpc on the right in the lower plots. This discontinuity occurs due to the slightly smaller value of the screening radius in the NFW case compared to that of the multi-component model.

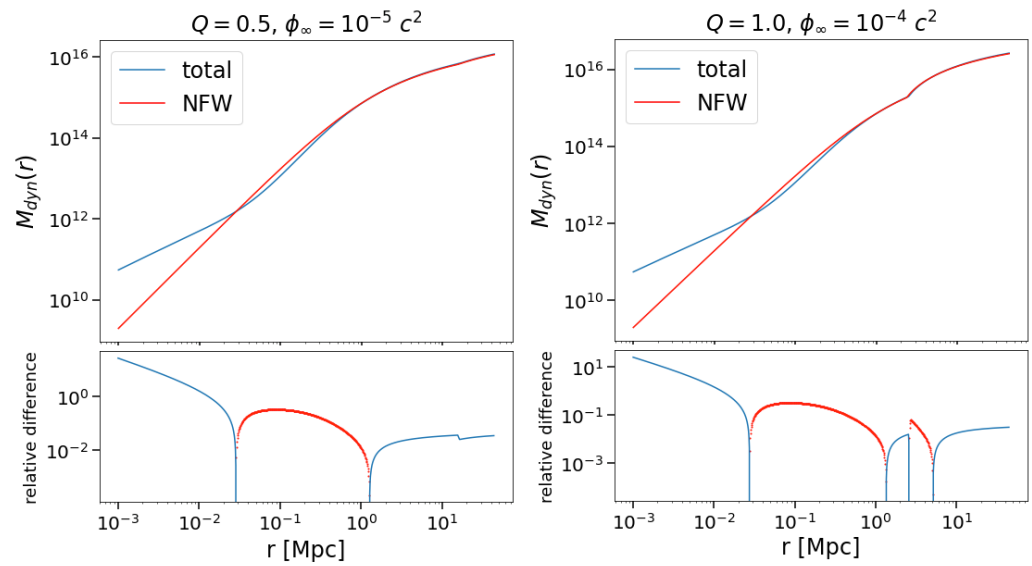


Figure 2. Top: total dynamical mass Equation (12), for a NFW case (red) and the multi-component profile (blue), for two values of the coupling parameter and background field (left and right). Bottom: relative difference between the single and the multi-component profile. The parameters adopted for the mass components are $\rho_s = 3.97 \times 10^{14}$; $r_s = 0.87$ Mpc; $\gamma = 0.7$; $\rho_* = 3.55 \times 10^{13} M_{\odot}/\text{Mpc}^3$; $r_* = 0.36$ Mpc; $\rho_g = 2.54 \times 10^{14} M_{\odot}/\text{Mpc}^3$; $r_g = 0.37$ Mpc; $\rho_b = 10^{15} M_{\odot}/\text{Mpc}^3$; $r_j = 0.03$ Mpc.

4. Validation with Numerical Solutions

In order to validate the approach described in Section 3, let us compare the solutions obtained through the semi-analytical approach with the ones obtained via numerically solving Equation (5).

The numerical solution of Equation (5) was obtained through a 6th-order explicit Runge–Kutta integrator with the appropriate boundary conditions⁶ imposed through a Newton–Raphson root-finding method. An inner cutoff radius was imposed to avoid the divergence present at the centre of the mass density profiles of the BCG, baryonic mass in galaxies, and CDM models. To obtain the best fit for the semi-analytic approach, the value of the latter ranged between 1 and 10% of the screening radius, S . The appropriate boundary condition at infinity was imposed by considering a numerically small value of the scalar field derivative, $\sim 10^{-8}$, at a scaled radius $x \equiv r/S$, which is several times larger than the size of the main mass distribution, $x_{\text{max}} \approx 10^3$.

Comparative results between the semi-analytic (solid) and the full numerical solutions (points) can be seen in Figure 3 for the multi-component mass density model, assuming the mass configuration presented in Section 3.1 (Figure 2) and then varying the chameleon and density parameters.

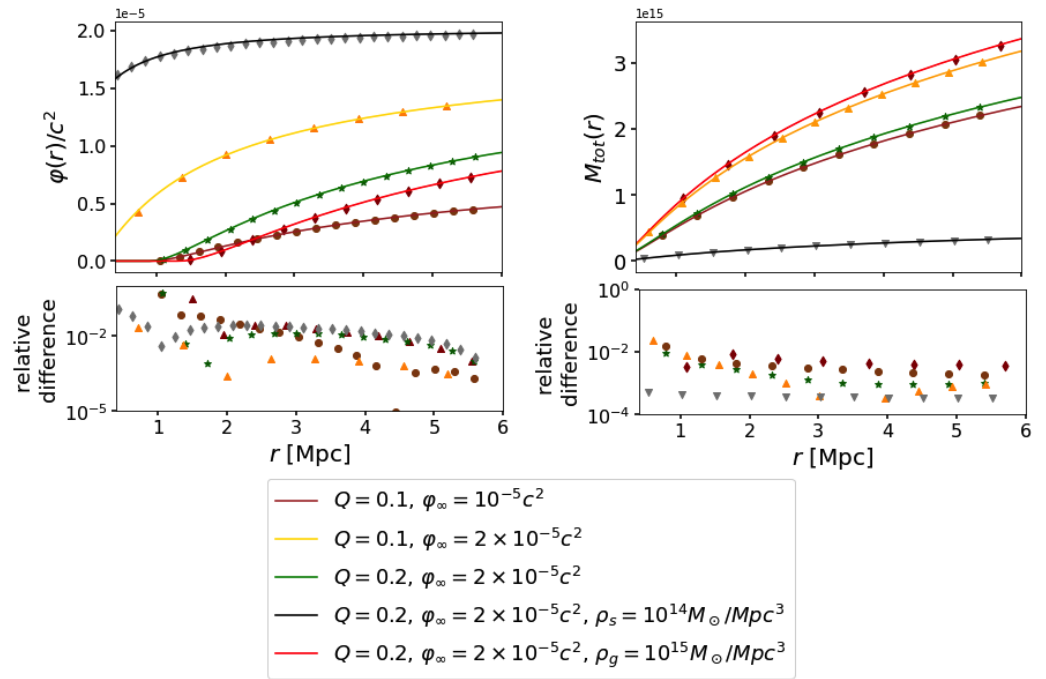


Figure 3. Left: Semi-analytic approximation of the radial field profile $\varphi(r) = \phi/M_{\text{Pl}}$ (solid lines) compared with the numerical solution (points) for different values of the mass profile parameters. The bottom plot indicates the relative difference between the two. Right: The same approximation when applied to the total dynamical mass $M_{\text{tot}} = M + M_{\text{eff}}$. The parameters adopted are $\rho_s = 3.97 \times 10^{14}$; $r_s = 0.87$ Mpc; $\gamma = 0.7$; $\rho_* = 3.55 \times 10^{13} M_\odot/\text{Mpc}^3$; $r_* = 0.36$ Mpc; $\rho_g = 2.54 \times 10^{14} M_\odot/\text{Mpc}^3$; $r_g = 0.37$ Mpc; $\rho_b = 10^{15} M_\odot/\text{Mpc}^3$; and $r_J = 0.03$ Mpc.

In Figure 3, both the scalar field profile (top left) and the total mass (top right) are represented, as well as the respective relative difference between the semi-analytically and numerically obtained solutions (bottom).

To determine how well the semi-analytical solution describes the true behaviour of the scalar field, let us analyse the relative difference in the scalar field profile (bottom left). In the region inside the screening radius S , $x \in [0, 1]$ —where the strongest assumptions/approximations were made—when the semi-analytical was set to zero, the numerical solutions were small but non-zero. This leads to a large relative difference, which is accentuated at the transitional scaled radius x_S , where the numerics gain significant non-zero values before the semi-analytical (smoother transition from a negligible value). This behaviour is, however, stopped as one moves away from the mass distribution ($x > 1$) to the background configuration (no mass distribution; flat scalar field profile). At this point, the semi-analytical and numerically obtained solutions coincide almost perfectly, with a maximum relative error of 10^{-3} .

Therefore, besides some slight differences in the screening radius transition and asymptotic behaviour, the semi-analytic approximation describes the numerically obtained results with a high degree of accuracy, providing confidence in their use in the more complex calculations that will proceed from this.

5. Constraints on Chameleon Gravity with Kinematics and Lensing Analyses of Galaxy Clusters

In what follows, we simulate the kinematic and lensing information of a galaxy cluster, as provided by a realistic current and upcoming surveys. The aim is to forecast the constraints on (ϕ_∞, Q) obtained when considering a multi-component mass reconstruction of the cluster. As was carried out in, e.g., [34,40], the analysis will be performed in terms of the scaled chameleon parameters $Q_2 = Q/(1 + Q)$ and $\phi_2 = 1 - \exp[\phi/(10^4 M_{\text{Pl}})]$, with the range $[0, 1]$.

Following the procedure presented in [41], we generate a mock spherically symmetric, dynamically relaxed distribution of particles resembling an isolated galaxy cluster by using an updated version of the *ClusterGEN* code [61]. The features of this synthetic halo mimic the structure of MACS 1206, which will be the future target of the analysis presented here. We populated the halo with $\sim 7r_{200}^{(\text{tot})}$ —at which point we set $r_{200}^{(\text{tot})} = 2.15$ Mpc, see Section 3.1—considering 380 particles (*aka* galaxies) within a sphere of $r_{200}^{(\text{tot})}$; in this way, we obtained 477 particles in a cylinder of (projected) radius $R = r_{200}^{(\text{tot})}$, which is close to the number of galaxies in the reference sample of [49]. The particles were distributed according to their NFW number density profile $\nu(r) = \nu_{\text{NFW}}(r, r_v)$, where the scale radius was $r_v = 0.46$ Mpc, corresponding to the best fit quoted in [49] for the same sample. For each component of the mass profile, we assumed the values of the parameters displayed in Section 3.1.

Every galaxy (particle) at a three-dimensional distance r from the cluster centre was assigned a velocity dispersion along the radial direction, $\sigma_r^2(r)$, provided by the solution of the *Jeans' equation*:

$$\frac{d(\nu\sigma_r^2)}{dr} + 2\beta(r)\frac{\nu\sigma_r^2}{r} = -\nu(r)\frac{d\Phi}{dr}. \tag{25}$$

where Φ is the total gravitational potential and $\beta(r) \equiv 1 - (\sigma_\theta^2 + \sigma_\phi^2)/2\sigma_r^2$ is the velocity anisotropy profile; σ_θ^2 and σ_ϕ^2 are the velocity dispersion components along the tangential and azimuthal directions, respectively. Under the assumption of spherical symmetry, $\sigma_\theta^2 = \sigma_\phi^2$, and the anisotropy profile simplifies to $\beta(r) = 1 - \sigma_\theta^2/\sigma_r^2$. The mock halo is simulated assuming a generalization of the Tiert model [62] for $\beta(r)$ (β_{gT} hereafter; see [63]):

$$\beta_{gT}(r) = \beta_0 + (\beta_\infty - \beta_0)\frac{r}{r + r_\beta}, \tag{26}$$

where r_β is a scale radius that is assumed to be equal to $r_{-2} = (2 - \gamma)r_s$ of the CDM density profile [49]; $\beta_0 = 0.5$, $\beta_\infty = 0.9$ are the values of the anisotropy at the centre and large radii, respectively, again chosen to mimic the radial anisotropy reconstructed for MACS 1206. Note that β_{gT} can range from $-\infty$, for purely tangential orbits to 1, for purely radial orbits. In what follows, let us define $\mathcal{A}_{0,\infty} = (1 - \beta_{0,\infty})^{-1/2}$, which is strictly positive— $(0, \infty)$ —and $> (<)1$ for the radial (tangential) anisotropy, and $= 1$ for isotropic orbits.

From the anisotropy value of r , the tangential (and azimuthal) velocity dispersion is given by

$$\sigma_\theta^2(r) \equiv \sigma_\phi^2(r) = [1 - \beta(r)]\sigma_r^2(r). \tag{27}$$

Each component of the rest-frame velocities of particles can then be obtained via sampling using a Gaussian distribution $\mathcal{G}(\mu, \sigma_j)$, where $\mu = 0$ and $j = \{r, \theta, \phi\}$.

Along with the spatial (and momentum) distribution of the member galaxies in the synthetic cluster, a line-of-sight VDP of the stars in the BCG was simulated for six points in the projected radius R from the centre of the galaxy, which are assumed to coincide with the centre of the cluster. The line-of-sight VDP of the BCG will be denoted as $\sigma_{\text{BCG}}^2(R)$. As shown in, e.g., [51], in Equations (10) and (11), the VDP of the BCG depends on the gravitational potential sourced by all matter components.

In the left panels of Figure 4, the simulated VDP is shown for the two sets of mock data considered in this analysis: Newtonian gravity, $\phi_\infty = Q = 0$ (hereafter, **case I**) and a strong chameleon scenario $\phi_\infty/M_{\text{Pl}} = 10^{-4}c^2$ and $Q = 1.0$, as in [41] (hereafter, **case II**). These values correspond to $\phi_2 = 0.63$, $Q_2 = 0.5$. Note that the VDP of the BCG is identical in both cases due to the large screening radius, $S = 2.63$ Mpc, which suppresses the dynamics of the fifth force at the BCG scale (i.e., the galaxy is completely screened).

For the uncertainties, we consider a 5% error for each point, which is consistent with the uncertainties in the observational data used in [49].

To constrain the chameleon parameters in the mock cluster data, an upgraded version of the MG-MAMPOST⁷ (accessed on 20 November 2024). code (see [61,64]) is employed.

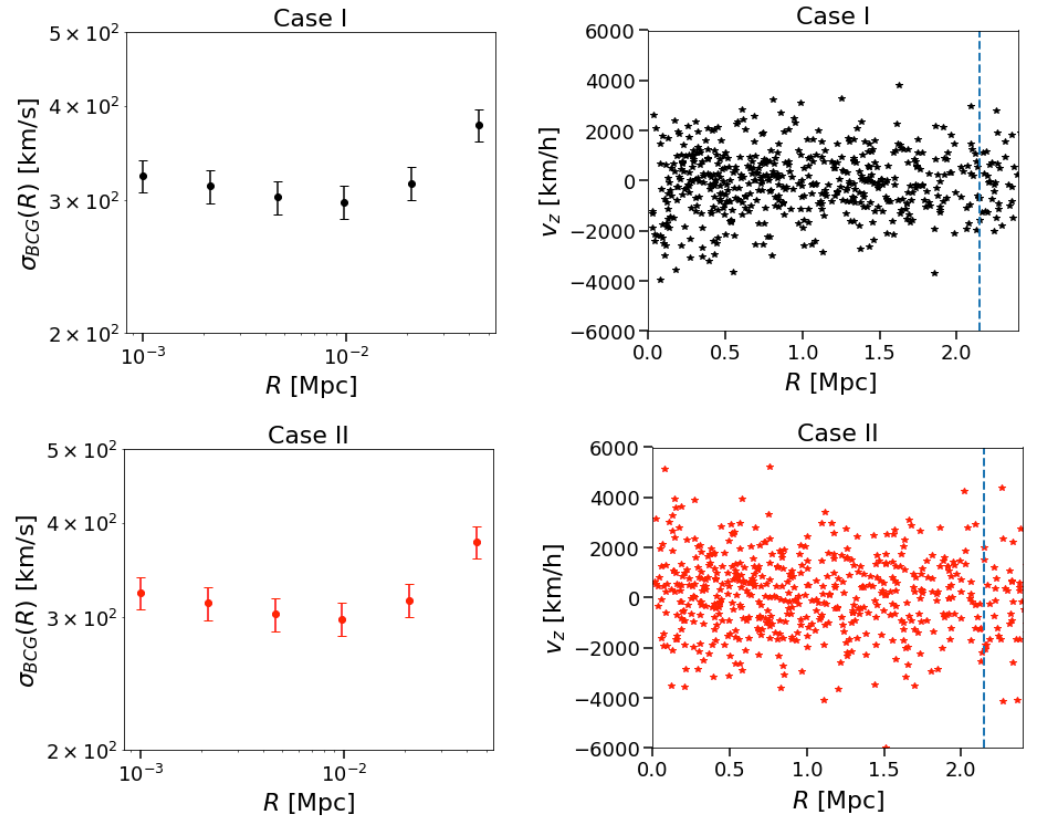


Figure 4. Mock data of the VDP along the line-of-sight for the BCG (**left**) and projected phase-space of member galaxies (**right**) for a multi-component modelled cluster generated assuming Newtonian gravity (**top**) and a chameleon universe with $\phi_\infty/M_{\text{Pl}} = 10^{-4} c^2$ and $Q = 1.0$ (**bottom**). The vertical blue dashed lines indicate the values of $r_{200}^{(\text{tot})} = 2.15$ Mpc.

Based on the MAMPOSST method of [65], MG-MAMPOSST performs a parametric reconstruction of the gravitational potential, $\Phi(r)$, the anisotropy $\beta(r)$, and the number density $\nu(r)$ profiles of spherically symmetric systems by solving the Jeans' equation in Newtonian gravity or some general class of modified gravity. Specifically, the code performs a Monte Carlo Markov Chain (MCMC) sampling of the parameter space, with the projected phase-space (pps) of member galaxies as the input data. The set of couples is $(R^{(i)}, v_z^{(i)})$, where $R^{(i)}$ is the projected position of a galaxy with respect to the centre of the cluster and $v_z^{(i)}$ is the velocity measured along the line-of-sight (los).

In Figure 4 (right), the pps extracted from the synthetic clusters of case I (top) and case II (bottom) are shown. Note that, in general, the modified gravity scenario predicts a larger los velocity dispersion of member galaxies than in the Newtonian case.

The MG-MAMPOSST log-likelihood is given by

$$\mathcal{L}_{\text{MAM}}(\Theta) = \sum_i \ln q(R_i, v_{z,i} | \Theta), \quad (28)$$

where $q(R^{(i)}, v_z^{(i)} | \Theta)$ is the probability of finding a galaxy at the point $R^{(i)}, v_z^{(i)}$. The sum covers the particles in the pps, and Θ is the vector of the parameters describing the model; in our case, $\Theta \in \{r_{200}, r_s, X_L, r_J, \phi_\infty, Q\}$, with $X_L = M_*/L_*$ the ratio between the stellar mass and the total luminosity of the BCG in a given band. Following the method used in [49], let us assume $L_* = 4.9 \times 10^{11} L_\odot$ in the I -band. Note that ρ_g, r_g, ρ_* and r_* are fixed to the best fit values quoted in Section 3.1. It was further checked that variations in these parameters within the range of uncertainties does not lead to considerable changes in the results of our analysis.

In addition to the pps, MG-MAMPOSST is equipped with a module to fit the observed VDP of the BCG, such that the total kinematic log-likelihood is

$$\mathcal{L}_{\text{kin}}(\Theta) = \mathcal{L}_{\text{MAM}}(\Theta) - \frac{\chi_{\text{BCG}}(\Theta)}{2}, \tag{29}$$

with $\chi_{\text{BCG}}(\theta)$ the chi-square obtained by comparing the theoretical prediction of $\sigma_{\text{BCG}}^2(R_j)$ with the observed data points $\sigma_{\text{obs},j}^2$ at R_j .

As for the priors, we first considered broad, uninformative flat priors for all the free parameters in the analysis of both case I and case II, with the upper and lower bounds provided in the second and third columns of Table 1. Note that for the BCG stellar mass-to-light ratio, we considered the bounds provided by the two- σ region from the analysis of [49].

The marginalized probability distributions of the chameleon parameters, resulting from a 110,000 points-MCMC sampling of \mathcal{L}_{kin} ,⁸ are shown in the left (case I) and right (case II) panels of Figure 5. For comparison, the dashed lines represent the results obtained when the total mass of the cluster is modelled as a single NFW profile (in this case, no BCG data are considered).

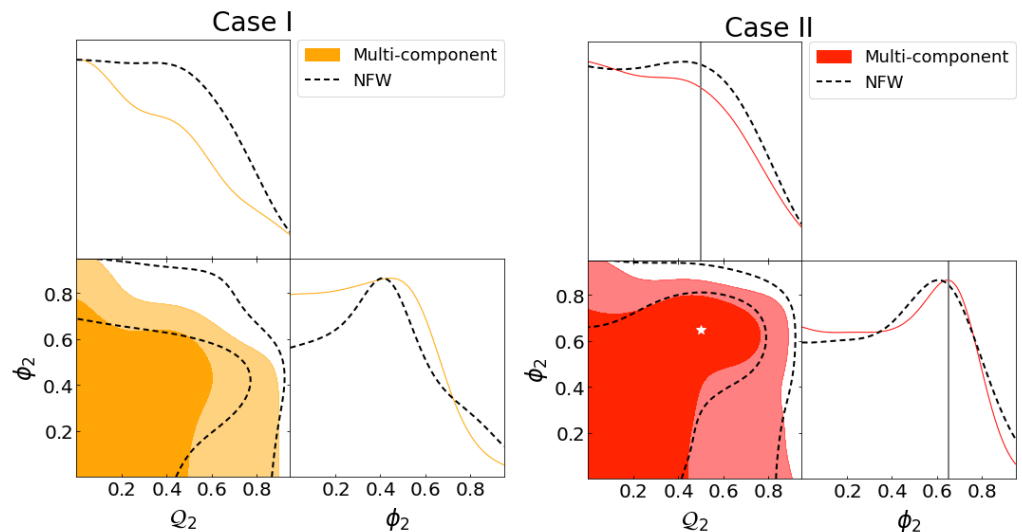


Figure 5. Solid lines: marginalized distributions of ϕ_2 and Q_2 from the MG-MAMPOSST analysis of the cluster in Newtonian gravity (left) and chameleon gravity with $Q_2 = 0.5$ and $\phi_2 = 0.63$ (right). The white star and the vertical solid lines on the right plots indicate the true values of the chameleon parameters. The inner and outer shaded regions represent the one- σ and two- σ contours in the parameter space, respectively. Dashed line: distribution obtained when considering a single NFW mass profile to model the total mass distribution in the MG-MAMPOSST fit.

As was shown in [41] for a single mass model, the constraints for case I agree with GR expectation ($\phi_2 = Q_2 = 0$) within one- σ . The contour of the single NFW slightly differs from that of the correct multi-component model; the only relevant changes that occurred due to the addition of the BCG data to the kinematic analysis were for the region in the top right section of the parameter space (ϕ_2, Q_2). Indeed, while it is true that the BCG VDP data are very powerful in constraining the central region of the cluster, including the slope of the mass profile—as shown in the triangle plots in Appendix A—at a small r , the cluster is supposed to be screened, except for very large values of ϕ_2 and Q_2 (i.e., the top right part of the two-dimensional contour plots in Figure 5).

In case II, even if the true values of the chameleon parameters sit well inside the one- σ region of the marginalized distribution, no evidence of departure from standard gravity can be claimed from the MG-MAMPOSST analysis. This is not surprising; as was shown in previous works (e.g., [40,41,61]), kinematic data in clusters cannot provide bounds in the

chameleon space if no additional information is provided. The reason for this is the quite strong degeneracy between the total cluster size (represented by the freedom in r_{200} of the CDM profile), Q_2 and ϕ_2 , as shown in Figure A1.

For this reason, we repeated the analysis by assuming a Gaussian prior on the CDM profile parameters $\mathcal{G}(r_{200}, r_s)$ (note that the flat prior on the gNFW exponent γ is unaltered), centred on the true values, which mimic the availability of a gravitational lensing survey. Following the advice of [41], we considered reliable uncertainties, given the current lensing-like mass reconstruction [66] $\sigma_{r_{200}} = 0.1 r_{200}$ and $\sigma_{r_s} = 0.3 r_s$, since the photon path is unaffected by the fifth force in chameleon gravity. The gravitational lensing determinations of the total cluster’s mass are thus only sensitive to the Newtonian part of the effective mass profile (e.g., [67]).

Table 1. Prior values for the free parameters in the MG-MAMPOSST analysis (kinematic only).

Parameter	Lower Bound	Upper Bound
r_{200}	0.5 Mpc	5.0 Mpc
r_s	0.05 Mpc	5.0 Mpc
γ	0	2
\mathcal{A}_∞	0.5	5.5
\mathcal{A}_0	0.5	5.5
X_L	4.20	4.74
ϕ_2	0	1
Q_2	0	1

Figure 6 shows the marginalized distributions for Q_2 and ϕ_2 when the “lensing” prior is applied in the MCMC MG-MAMPOSST run. Again, the dashed lines refer to a cluster with the same $r_{200}^{(tot)}$ and $r_{-2}^{(tot)}$, modelled using a single NFW profile.⁹ Interestingly, for case I, no relevant changes were obtained with the inclusion of additional information in the multi-component model. This is mainly due to the large values of Q_2 and ϕ_2 that were already excluded by the BCG VDP, as mentioned above. Note that the result of the NFW model + lensing is now almost identical to that of the multi-component case, confirming the effects of the Gaussian prior to cutting the top part of the parameter space.

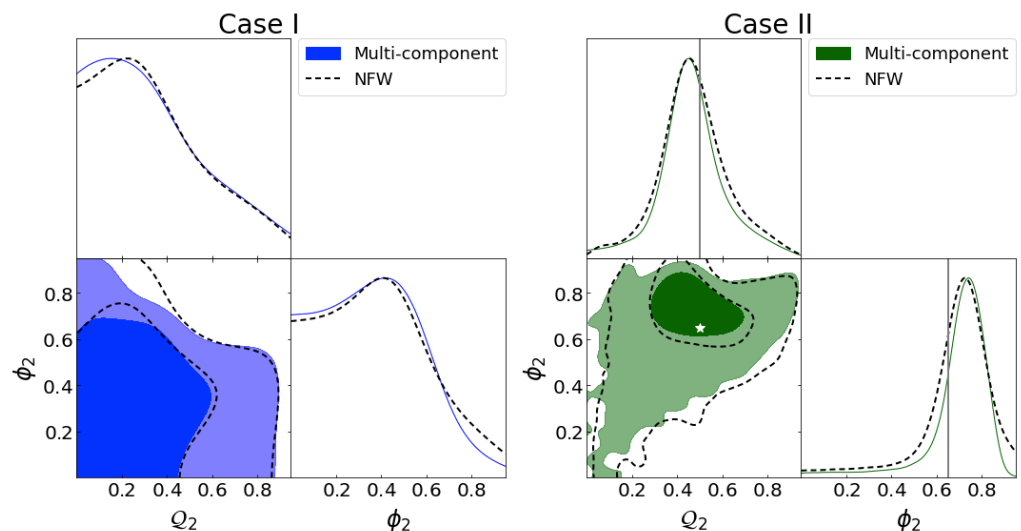


Figure 6. The same setup as Figure 5, but including a Gaussian (lensing) prior on r_{200} and r_s of the CDM profile. Solid lines/filled areas: cluster where all the mass components are explicitly modelled. Dashed lines/contours: single NFW-modeled cluster. The white star and the vertical solid lines on the right plots indicate the true values of the chameleon parameters.

However, the lensing information is required to distinguish the strongly modified gravity scenario, where the combination of the MG-MAMPOSST analysis plus the prior enhances the probability regarding the true values of the chameleon parameters (see the right panel of Figure A2). For this specific case, we obtained $Q_2 = 0.47^{+0.34}_{-0.33}$ and $\phi_2 = 0.70^{+0.22}_{-0.34}$ for the multi-component profile.

Finally, as shown in Figure A4, in clusters with strong MG signatures, the chameleon parameters exhibit a correlation with the anisotropy profile in the innermost regions of the cluster, which is absent in the standard scenario.

6. Conclusions

This manuscript presents a semi-analytical approach for describing the chameleon field in realistically modelled galaxy clusters. A particular focus was placed on the screening mechanism and the behaviour of the chameleon fifth force when each matter component of a cluster was modelled using its individual best descriptor instead of a single model describing the total mass profile.

The total galaxy cluster's mass density profile was first decomposed into four components: the BCG, the baryonic mass in galaxies, the ICM, and the CDM component. The BCG was described assuming a Jaffe profile and the ICM using an Isothermal beta model, while NFW and gNFW profiles described the baryonic components in galaxies and the diffuse CDM, respectively. The semi-analytic expressions for the effective mass profile and the radial field profile were derived under spherical symmetry and tested against full numerical solutions.

The semi-analytical approach was then implemented in the MG-MAMPOSST code of [64], which constrains modified gravity models at cluster scales with kinematics analyses of the member galaxies, assuming spherical symmetry and dynamical relaxation. As discussed in [41], the advantage of the semi-analytic approximation relies on the reduced computational time with respect to the numerical computation while still yielding the same accuracy. This makes it suitable for statistical inference and a fast exploration of the parameter space.

Using mock data—based on the real massive galaxy cluster MACS 1206 at $z = 0.44$ —we forecast the obtainable bounds via a combination of the pps data of galaxies, BCG (projected) VDP, and additional lensing-like information on the CDM profile parameters r_{200} , r_s . While for a GR cluster, the MG-MAMPOSST analysis including BCG data is sufficient to break the degeneracy among mass profiles and chameleon parameters (excluding the large (Q_2 , ϕ_2) part of the parameter space, contrary to what occurs for a single mass model without the BCG data), in a modified gravity cluster, a joint lensing+kinematic analysis is required to provide constraints on Q_2 and ϕ_2 .

The results from a multi-component-modelled cluster were further compared with those obtained from a single NFW-modelled halo with the same total mass at $r = r_{200}^{(\text{tot})}$. Interestingly, the larger improvement in the constraints from the former derives from the possibility of including the BCG VDP data—which can be only used on an explicit model of the BCG stellar mass profile—in the kinematic analysis.

It is important to point out that the study performed here assumes clusters in dynamical equilibrium, and the mass components follow a spherical smooth distribution. As pointed out in [37], large deviations from spherical symmetry may impact the effect of the fifth force; moreover, in [68], the lack of dynamical relaxation was shown to be a relevant source of systematic effects for kinematics mass reconstructions in modified gravity. However, MACS 1206, which was the target of the analysis presented here, is a well-studied relaxed cluster with a nearly concentric mass distribution, as pointed out in several works (e.g., [49,69,70]).

Along with kinematics and lensing, X-ray data can be used to further constrain a cluster's mass profiles assuming hydrostatic equilibrium in both GR ([71]) and in MG (e.g., [34,40]). As discussed in [61], even if gas and galaxies "feel" the same gravitational potential, their physics are different, and so is the degeneracy among the model parameters. Thus, in an upcoming work, the analysis presented here will be extended to include X-ray information. The constraining power of the joint kinematics, lensing and X-ray data will be explored and tested on a real cluster.

Note that while the discussion here focused on the chameleon model, the method can easily be extended to many alternative scenarios, such as other viable models in the Horndeski sector (e.g., [72]) or the more general Degenerate-Higher-Order Scalar-Tensor Theories (DHOST [73–75]), for which constraints at different scales have recently been derived in the literature (e.g., [25,26,52,76]). The formalism developed here to simultaneously assess the inner- and outermost regions of a galaxy cluster is crucial to test scenarios where non-local interactions are present; for instance, the non-minimal coupling of dark matter to gravity [77–79] or fractional gravity [80]. Understanding the characteristic signature of different MG models on a cluster's mass profile determinations is critical in the context of current and upcoming imaging and spectroscopic surveys at several wavelengths, both ground-based (e.g., Vera Rubin Observatory¹⁰) and in space (Euclid [81], JWST [82], Athena X-ray survey [83]), in order to provide a robust independent probe of possible alternatives to the Λ CDM scenario.

Author Contributions: The design of the research project is due to L.P., who implemented the code modification and developed the data analysis. The semi-analytic model was developed by V.A. under the supervision of L.P. The numerical solutions were obtained by A.M.P., who further helped in the writing and the final revision of the analysis. S.H. contributed with the interpretation of the results and with the final revision of the paper. All authors have read and agreed to the published version of the manuscript.

Funding: This study is supported by the Italian Ministry for Research and University (MUR) under Grant 'Progetto Dipartimenti di Eccellenza 2023-2027' (BiCoQ). AMP is supported by the Czech Science Foundation (GACR) project PreCOG (Grant No. 24-10780S).

Data Availability Statement: The previous version of the MG-MAMPOSS code is publicly available at <https://github.com/Pizzuti92/MG-MAMPOSS> (accessed on 20 November 2024). The auxiliary code CLUSTERGEN can be provided to the user upon specific request.

Conflicts of Interest: The authors declare no conflicts of interest. The funders had no role in the design of the study; in the collection, analyses, or interpretation of data; in the writing of the manuscript; or in the decision to publish the results.

Appendix A. Marginalized Distributions from the Analysis of the Mock Clusters

In the following, the marginalized distributions of all parameters in the MG-MAMPOSS MCMC runs are displayed. In each plot, two-dimensional inner and outer shaded regions correspond to one- σ and two- σ regions, respectively.

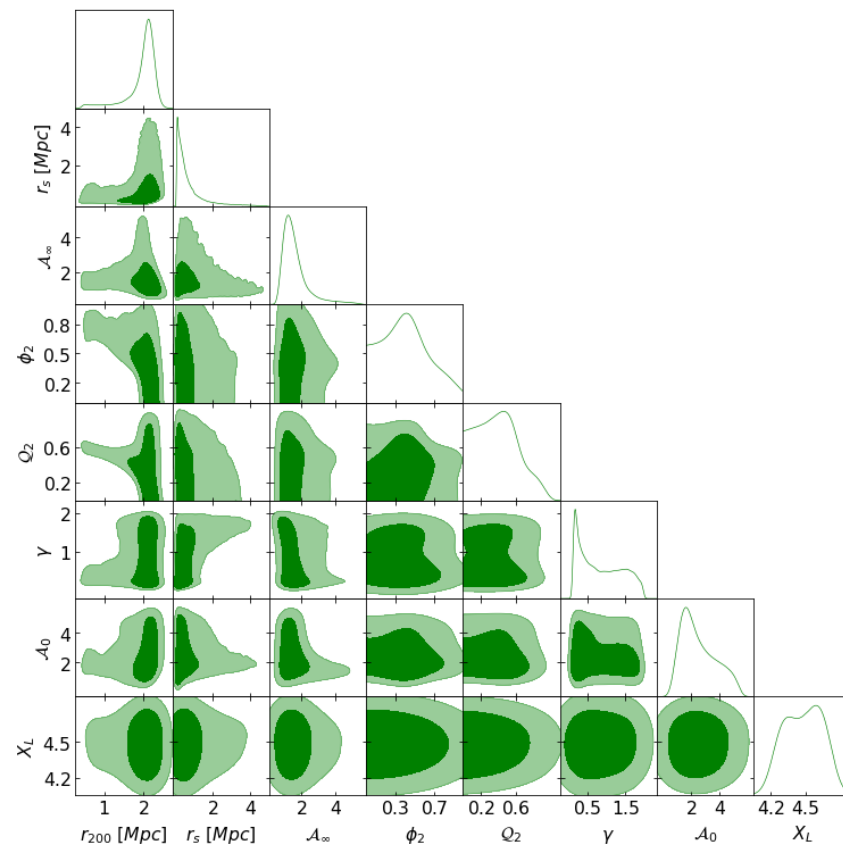


Figure A1. GR cluster, MG-MAMPOSST, only pps of member galaxies.

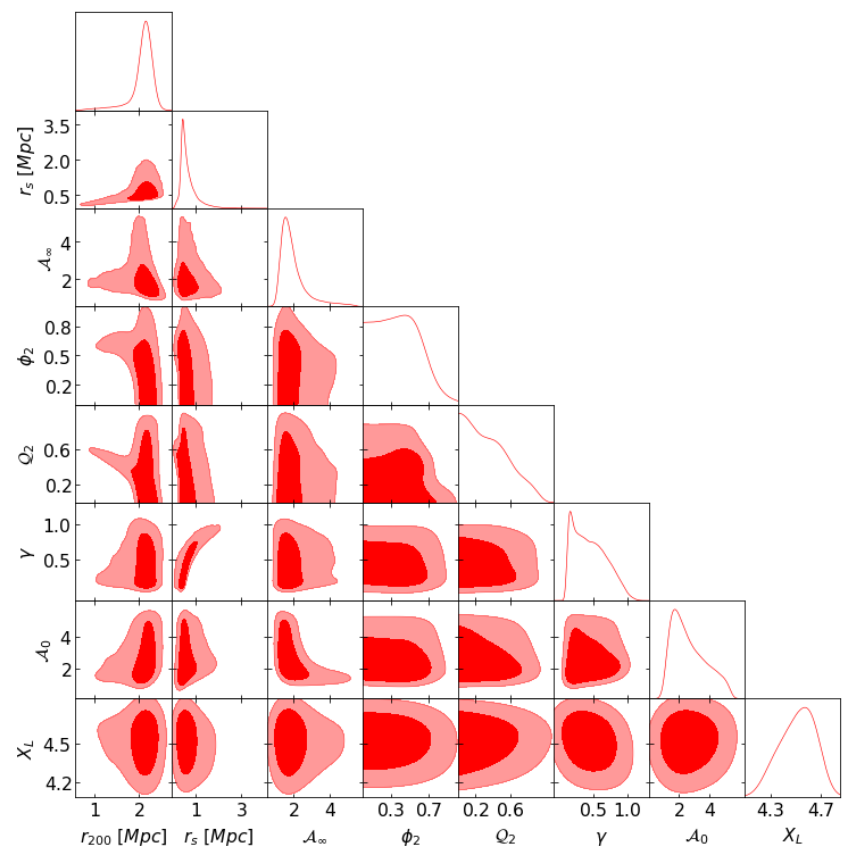


Figure A2. GR cluster, MG-MAMPOSST, pps+BGC VDF.

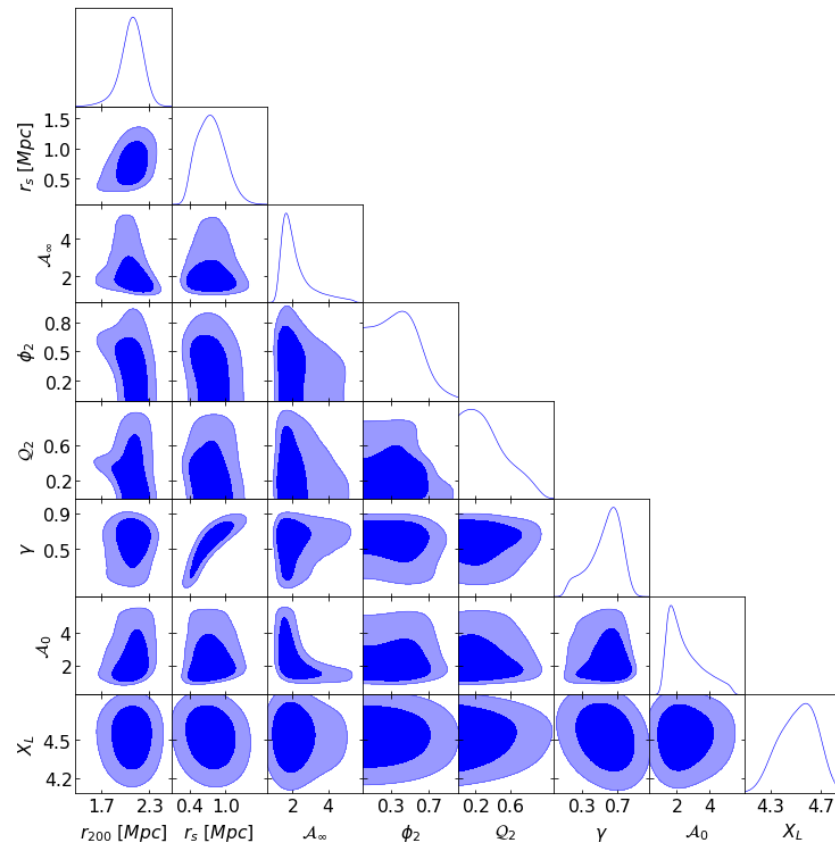


Figure A3. GR cluster, MG-MAMPOSST, pps+BGC VDP + lensing prior.

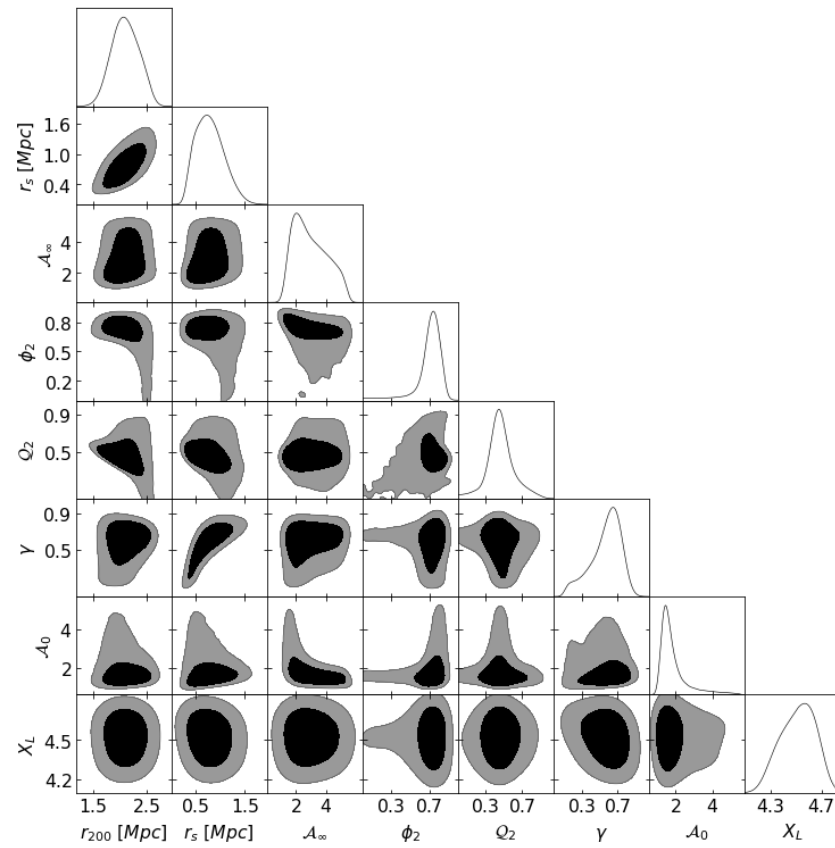


Figure A4. MG cluster, MG-MAMPOSST, pps+BGC VDP + lensing prior.

Notes

- 1 Note that the value $Q = 1/\sqrt{6}$, corresponds to the $f(\mathcal{R})$ models of gravity [45,46].
- 2 While it is possible to extend the analysis to distinct field couplings to the chameleon field, this is not the objective of the manuscript and will be explored in future investigations.
- 3 The standard NFW case was recovered for $\gamma = 1$.
- 4 Note the superscript (tot) is being used here to distinguish from r_{200} of the dark matter mass density profile.
- 5 The mass profile of member galaxies was obtained from [55]. The gas mass was provided by A. Biviano from S. Ettori via private communication.
- 6 Namely, $\nabla^2\phi \approx 0$ at the centre of the mass distribution and $d\phi/dr = 0$ at infinity.
- 7 A previous version of the code is publicly available at <https://github.com/Pizzuti92/MG-MAMPOSSt>.
- 8 The exploration of the parameter space was meticulously performed using a Metropolis–Hastings algorithm, with the first 10,000 points considered as burn-in phase.
- 9 In this case, the Gaussian priors are centred on $r_{200}^{(tot)}$ and $r_{-2}^{(tot)}$, with the same relative uncertainties.
- 10 <https://www.lsst.org/about> (accessed on 29 November 2024).

References

1. Riess, A.G.; Filippenko, A.V.; Challis, P.; Clocchiatti, A.; Diercks, A.; Garnavich, P.M.; Gilliland, R.L.; Hogan, C.J.; Jha, S.; Kirshner, R.P.; et al. Observational Evidence from Supernovae for an Accelerating Universe and a Cosmological Constant. *Astron. J.* **1998**, *116*, 1009–1038. [CrossRef]
2. Solanki, R.; De, A.; Mandal, S.; Sahoo, P. Accelerating expansion of the universe in modified symmetric teleparallel gravity. *Phys. Dark Universe* **2022**, *36*, 101053. [CrossRef]
3. Weinberg, S. The cosmological constant problem. *Rev. Mod. Phys.* **1989**, *61*, 1–23. [CrossRef]
4. Bull, P.; Akrami, Y.; Adamek, J.; Baker, T.; Bellini, E.; Beltrán Jiménez, J.; Bentivegna, E.; Camera, S.; Clesse, S.; Davis, J.H.; et al. Beyond Λ CDM: Problems, solutions, and the road ahead. *Phys. Dark Universe* **2016**, *12*, 56–99. [CrossRef]
5. Perivolaropoulos, L.; Skara, F. Challenges for Λ CDM: An update. *New Astron. Rev.* **2022**, *95*, 101659. [CrossRef]
6. Planck Collaboration; Adam, R.; Ade, P.A.R.; Aghanim, N.; Akrami, Y.; Alves, M.I.R.; Argüeso, F.; Arnaud, M.; Arroja, F.; Ashdown, M.; et al. Planck 2015 results—I. Overview of products and scientific results. *Astron. Astrophys.* **2016**, *594*, A1. [CrossRef]
7. Planck Collaboration; Ade, P.A.R.; Aghanim, N.; Arnaud, M.; Ashdown, M.; Aumont, J.; Baccigalupi, C.; Banday, A.J.; Barreiro, R.B.; Bartlett, J.G.; et al. Planck 2015 results—XIII. Cosmological parameters. *Astron. Astrophys.* **2016**, *594*, A13. [CrossRef]
8. The FADE Collaboration; Bernardo, H.; Bose, B.; Franzmann, G.; Hagstotz, S.; He, Y.; Litsa, A.; Niedermann, F. Modified gravity approaches to the cosmological constant problem. *arXiv* **2022**, arXiv:2210.06810.
9. Nojiri, S.; Odintsov, S.; Oikonomou, V. Modified gravity theories on a nutshell: Inflation, bounce and late-time evolution. *Phys. Rep.* **2017**, *692*, 1–104. [CrossRef]
10. Clifton, T.; Ferreira, P.G.; Padilla, A.; Skordis, C. Modified gravity and cosmology. *Phys. Rep.* **2012**, *513*, 1–189. [CrossRef]
11. Moffat, J.W. Scalar–tensor–vector gravity theory. *J. Cosmol. Astropart. Phys.* **2006**, *2006*, 004. [CrossRef]
12. Peracaula, J.S.; Gómez-Valent, A.; de Cruz Pérez, J.; Moreno-Pulido, C. Brans–Dicke Gravity with a Cosmological Constant Smooths Out Λ CDM Tensions. *Astrophys. J. Lett.* **2019**, *886*, L6. [CrossRef]
13. Hu, W.; Sawicki, I. Models of $f(R)$ cosmic acceleration that evade solar system tests. *Phys. Rev. D—Part. Fields Gravit. Cosmol.* **2007**, *76*, 064004. [CrossRef]
14. Khoury, J. Les Houches Lectures on Physics Beyond the Standard Model of Cosmology. *arXiv* **2013**, arXiv:1312.2006.
15. Burrage, C.; Sakstein, J. Tests of chameleon gravity. *Living Rev. Relativ.* **2018**, *21*, 1–58. [CrossRef]
16. Brax, P.; van de Bruck, C.; Davis, A.; Green, A. Small scale structure formation in chameleon cosmology. *Phys. Lett. B* **2006**, *633*, 441–446. [CrossRef]
17. Brax, P.; Davis, A.C.; Li, B.; Winther, H.A.; Zhao, G.B. Systematic simulations of modified gravity: Chameleon models. *J. Cosmol. Astropart. Phys.* **2013**, *2013*, 029. [CrossRef]
18. Will, C.M. The Confrontation between General Relativity and Experiment. *Living Rev. Relativ.* **2014**, *17*, 4. [CrossRef]
19. Khoury, J. Theories of Dark Energy with Screening Mechanisms. *arXiv* **2010**, arXiv:1011.5909.
20. Kobayashi, T.; Hiramatsu, T. Relativistic stars in degenerate higher-order scalar-tensor theories after GW170817. *Phys. Rev.* **2018**, *D97*, 104012. [CrossRef]
21. Amendola, L.; Kunz, M.; Saltas, I.D.; Sawicki, I. Fate of Large-Scale Structure in Modified Gravity After GW170817 and GRB170817A. *Phys. Rev. Lett.* **2018**, *120*, 131101. [CrossRef]
22. Kimura, R.; Kobayashi, T.; Yamamoto, K. Vainshtein screening in a cosmological background in the most general second-order scalar-tensor theory. *Phys. Rev. D* **2012**, *85*, 024023. [CrossRef]
23. Bayarsaikhan, B.; Koh, S.; Tsedenbaljir, E.; Tumurtushaa, G. Constraints on dark energy models from the Horndeski theory. *J. Cosmol. Astropart. Phys.* **2020**, *2020*, 057. [CrossRef]

24. Bellini, E.; Cuesta, A.J.; Jimenez, R.; Verde, L. Constraints on deviations from Λ CDM within Horndeski gravity. *J. Cosmol. Astropart. Phys.* **2016**, *2016*, 053. [[CrossRef](#)]
25. Saltas, I.D.; Lopes, I. Obtaining Precision Constraints on Modified Gravity with Helioseismology. *Phys. Rev. Lett.* **2019**, *123*, 091103. [[CrossRef](#)] [[PubMed](#)]
26. Hiramatsu, T. CMB constraints on DHOST theories. *J. Cosmol. Astropart. Phys.* **2022**, *2022*, 035. [[CrossRef](#)]
27. Khoury, J.; Weltman, A. Chameleon cosmology. *Phys. Rev. D* **2004**, *69*, 044026. [[CrossRef](#)]
28. Pernot-Borràs, M.; Bergé, J.; Brax, P.; Uzan, J.P.; Métris, G.; Rodrigues, M.; Touboul, P. Constraints on chameleon gravity from the measurement of the electrostatic stiffness of the MICROSCOPE mission accelerometers. *Phys. Rev. D* **2021**, *103*, 064070. [[CrossRef](#)]
29. Burrage, C.; Copeland, E.J.; Hinds, E. Probing dark energy with atom interferometry. *J. Cosmol. Astropart. Phys.* **2015**, *2015*, 042. [[CrossRef](#)]
30. Fischer, H.; Käding, C.; Pitschmann, M. Screened Scalar Fields in the Laboratory and the Solar System. *Universe* **2024**, *10*, 297. [[CrossRef](#)]
31. Naik, A.P.; Puchwein, E.; Davis, A.C.; Arnold, C. Imprints of Chameleon $f(R)$ gravity on Galaxy rotation curves. *Mon. Not. R. Astron. Soc.* **2018**, *480*, 5211–5225. [[CrossRef](#)]
32. Benisty, D.; Brax, P.; Davis, A.C. Stringent pulsar timing bounds on light scalar couplings to matter. *Phys. Rev. D* **2023**, *107*. [[CrossRef](#)]
33. Desmond, H.; Ferreira, P.G. Galaxy morphology rules out astrophysically relevant Hu-Sawicki $f(R)$ gravity. *Phys. Rev. D* **2020**, *102*, 104060. [[CrossRef](#)]
34. Wilcox, H.; Bacon, D.; Nichol, R.C.; Rooney, P.J.; Terukina, A.; Romer, A.K.; Koyama, K.; Zhao, G.B.; Hood, R.; Mann, R.G.; et al. The XMM Cluster Survey: Testing chameleon gravity using the profiles of clusters. *Mon. Not. Roy. Astron. Soc.* **2015**, *452*, 1171–1183. [[CrossRef](#)]
35. Cataneo, M.; Rapetti, D.; Lombriser, L.; Li, B. Cluster abundance in chameleon $f(R)$ gravity I: Toward an accurate halo mass function prediction. *J. Cosmol. Astropart. Phys.* **2016**, *2016*, 024. [[CrossRef](#)]
36. Pizzuti, L.; Sartoris, B.; Amendola, L.; Borgani, S.; Biviano, A.; Umetsu, K.; Mercurio, A.; Rosati, P.; Balestra, I.; Caminha, G.B.; et al. CLASH-VLT: Constraints on $f(R)$ gravity models with galaxy clusters using lensing and kinematic analyses. *J. Cosmol. Astropart. Phys.* **2017**, *7*, 023. [[CrossRef](#)]
37. Tamosiunas, A.; Bridson, C.; Burrage, C.; Cui, W.; Moss, A. Chameleon screening depends on the shape and structure of NFW halos. *J. Cosmol. Astropart. Phys.* **2022**, *2022*, 047. [[CrossRef](#)]
38. Navarro, J.F.; Frenk, C.S.; White, S.D.M. The Structure of cold dark matter halos. *Astrophys. J.* **1996**, *462*, 563–575. [[CrossRef](#)]
39. Ettori, S.; Ghirardini, V.; Eckert, D.; Pointecouteau, E.; Gastaldello, F.; Sereno, M.; Gaspari, M.; Ghizzardi, S.; Roncarelli, M.; Rossetti, M. Hydrostatic mass profiles in X-COP galaxy clusters. *Astron. Astrophys.* **2019**, *621*, A39. [[CrossRef](#)]
40. Boumechta, Y.; Haridasu, B.S.; Pizzuti, L.; Butt, M.A.; Baccigalupi, C.; Lapi, A. Constraining chameleon screening using galaxy cluster dynamics. *Phys. Rev. D* **2023**, *108*, 044007. [[CrossRef](#)]
41. Pizzuti, L.; Boumechta, Y.; Haridasu, S.; Pombo, A.M.; Dossena, S.; Butt, M.A.; Benetti, F.; Baccigalupi, C.; Lapi, A. Mass Modeling and Kinematics of Galaxy Clusters in Modified Gravity. *J. Cosmol. Astropart. Phys.* **2024**, *2024*, 014. [[CrossRef](#)]
42. Terukina, A.; Lombriser, L.; Yamamoto, K.; Bacon, D.; Koyama, K.; Nichol, R.C. Testing chameleon gravity with the Coma cluster. *J. Cosmol. Astropart. Phys.* **2014**, *2014*, 013. [[CrossRef](#)]
43. Khoury, J.; Weltman, A. Chameleon fields: Awaiting surprises for tests of gravity in space. *Phys. Rev. Lett.* **2004**, *93*, 171104. [[CrossRef](#)] [[PubMed](#)]
44. Butt, M.A.; Haridasu, B.S.; Boumechta, Y.; Benetti, F.; Pizzuti, L.; Baccigalupi, C.; Lapi, A. Caustic and hydrostatic mass bias: Implications for modified gravity. *Phys. Rev. D* **2024**, *109*, 064006. [[CrossRef](#)]
45. Starobinsky, A.A. Disappearing cosmological constant in $f(R)$ gravity. *JETP Lett.* **2007**, *86*, 157–163. [[CrossRef](#)]
46. Oyaizu, H.; Lima, M.; Hu, W. Nonlinear evolution of $f(R)$ cosmologies. II. Power spectrum. *Phys. Rev. D* **2008**, *78*, 123524. [[CrossRef](#)]
47. Zhang, X.; Niu, R.; Zhao, W. Constraining the scalar-tensor gravity theories with and without screening mechanisms by combined observations. *Phys. Rev. D* **2019**, *100*, 024038. [[CrossRef](#)]
48. Laganá, T.F.; Durret, F.; Lopes, P.A.A. Physical properties of the X-ray gas as a dynamical diagnosis for galaxy clusters. *Mon. Not. R. Astron. Soc.* **2019**, *484*, 2807–2830. [[CrossRef](#)]
49. Biviano, A.; Pizzuti, L.; Mercurio, A.; Sartoris, B.; Rosati, P.; Ettori, S.; Girardi, M.; Grillo, C.; Caminha, G.B.; Nonino, M. CLASH-VLT: The Inner Slope of the MACS J1206.2-0847 Dark Matter Density Profile. *Astrophys. J.* **2023**, *958*, 148. [[CrossRef](#)]
50. Burrage, C.; Copeland, E.J.; Moss, A.; Stevenson, J.A. The shape dependence of chameleon screening. *J. Cosmol. Astropart. Phys.* **2018**, *01*, 056. [[CrossRef](#)]
51. Sartoris, B.; Biviano, A.; Rosati, P.; Mercurio, A.; Grillo, C.; Ettori, S.; Nonino, M.; Umetsu, K.; Bergamini, P.; Caminha, G.B.; et al. CLASH-VLT: A full dynamical reconstruction of the mass profile of Abell S1063 from 1 kpc out to the virial radius. *Astron. Astrophys.* **2020**, *637*, A34. [[CrossRef](#)]
52. Laudato, E.; Salzano, V.; Umetsu, K. Multi-component DHOST analysis in galaxy clusters. *arXiv* **2021**, arXiv:2110.11019.
53. Jaffe, W. A simple model for the distribution of light in spherical galaxies. *Mon. Not. R. Astron. Soc.* **1983**, *202*, 995–999. [[CrossRef](#)]

54. Sand, D.J.; Treu, T.; Smith, G.P.; Ellis, R.S. The Dark Matter Distribution in the Central Regions of Galaxy Clusters: Implications for Cold Dark Matter. *Astrophys. J.* **2004**, *604*, 88–107. [[CrossRef](#)]
55. Annunziatella, M.; Biviano, A.; Mercurio, A.; Nonino, M.; Rosati, P.; Balestra, I.; Presotto, V.; Girardi, M.; Gobat, R.; Grillo, C.; et al. CLASH-VLT: The stellar mass function and stellar mass density profile of the $z = 0.44$ cluster of galaxies MACS J1206.2-0847. *Astron. Astrophys.* **2014**, *571*, A80. [[CrossRef](#)]
56. Barrena, R.; Pizzuti, L.; Chon, G.; Böhringer, H. Unveiling the shape: A multi-wavelength analysis of the galaxy clusters Abell 76 and Abell 1307. *Astron. Astrophys.* **2024**, *691*, A135. [[CrossRef](#)]
57. King, I. The structure of star clusters. I. an empirical density law. *Astron. J.* **1962**, *67*, 471. [[CrossRef](#)]
58. Patej, A.; Loeb, A. A simple physical model for the gas distribution in galaxy clusters. *Astrophys. J. Lett.* **2014**, *798*, L20. [[CrossRef](#)]
59. Cao, S.; Biesiada, M.; Zheng, X.; Zhu, Z.H. Testing the gas mass density profile of galaxy clusters with distance duality relation. *Mon. Not. R. Astron. Soc.* **2016**, *457*, 281–287. [[CrossRef](#)]
60. Radiconi, F.; Vacca, V.; Battistelli, E.; Bonafede, A.; Capalbo, V.; Devlin, M.J.; Di Mascolo, L.; Feretti, L.; Gallardo, P.A.; Gill, A.; et al. The thermal and non-thermal components within and between galaxy clusters Abell 399 and Abell 401. *Mon. Not. R. Astron. Soc.* **2022**, *517*, 5232–5246. [[CrossRef](#)]
61. Pizzuti, L.; Saltas, I.D.; Amendola, L. MG-MAMPOSST: A code to test modifications of gravity with internal kinematics and lensing analyses of galaxy clusters. *Mon. Not. R. Astron. Soc.* **2021**, *506*, 595–612. [[CrossRef](#)]
62. Tiret, O.; Combes, F.; Angus, G.W.; Famaey, B.; Zhao, H.S. Velocity dispersion around ellipticals in MOND. *Astron. Astrophys.* **2007**, *476*, L1–L4. [[CrossRef](#)]
63. Mamon, G.A.; Cava, A.; Biviano, A.; Moretti, A.; Poggianti, B.; Bettoni, D. Structural and dynamical modeling of WINGS clusters. II. The orbital anisotropies of elliptical, spiral and lenticular galaxies. *Astron. Astrophys.* **2019**, *631*, A131. [[CrossRef](#)]
64. Pizzuti, L.; Saltas, I.D.; Biviano, A.; Mamon, G.; Amendola, L. MG-MAMPOSSt, a Fortran code to test gravity at galaxy-cluster scales. *J. Open Source Softw.* **2023**, *8*, 4800. [[CrossRef](#)]
65. Mamon, G.A.; Biviano, A.; Boué, G. MAMPOSSt: Modelling Anisotropy and Mass Profiles of Observed Spherical Systems—I. Gaussian 3D velocities. *Mon. Not. R. Astron. Soc.* **2013**, *429*, 3079–3098. [[CrossRef](#)]
66. Umetsu, K.; Zitrin, A.; Gruen, D.; Merten, J.; Donahue, M.; Postman, M. CLASH: Joint Analysis of Strong-Lensing, Weak-Lensing Shear and Magnification Data for 20 Galaxy Clusters. *Astrophys. J.* **2016**, *821*, 116. [[CrossRef](#)]
67. Schmidt, F.; Vikhlinin, A.; Hu, W. Cluster constraints on $f(R)$ gravity. *Phys. Rev. D* **2009**, *80*, 083505. [[CrossRef](#)]
68. Pizzuti, L.; Sartoris, B.; Borgani, S.; Biviano, A. Calibration of systematics in constraining modified gravity models with galaxy cluster mass profiles. *J. Cosmol. Astropart. Phys.* **2020**, *2020*, 024. [[CrossRef](#)]
69. Girardi, M.; Mercurio, A.; Balestra, I.; Nonino, M.; Biviano, A.; Grillo, C.; Rosati, P.; Annunziatella, M.; Demarco, R.; Fritz, A.; et al. CLASH-VLT: Substructure in the galaxy cluster MACS J1206.2-0847 from kinematics of galaxy populations. *Astron. Astrophys.* **2015**, *579*, A4. [[CrossRef](#)]
70. Ferrami, G.; Bertin, G.; Grillo, C.; Mercurio, A.; Rosati, P. Dynamics of the galactic component of Abell S1063 and MACS J1206. 2-0847. *Astron. Astrophys.* **2023**, *676*, A66. [[CrossRef](#)]
71. Ettori, S.; Donnarumma, A.; Pointecouteau, E.; Reiprich, T.; Giodini, S.; Lovisari, L.; Schmidt, R. Mass profiles of Galaxy Clusters from X-ray analysis. *Space Sci. Rev.* **2013**, *177*, 119–154. [[CrossRef](#)]
72. Variaschi, G.U. Newtonian Fractional-Dimension Gravity and MOND. *Found. Phys.* **2020**, *50*, 1608–1644. [[CrossRef](#)]
73. Koyama, K.; Sakstein, J. Astrophysical Probes of the Vainshtein Mechanism: Stars and Galaxies. *Phys. Rev.* **2015**, *D91*, 124066. [[CrossRef](#)]
74. Crisostomi, M.; Lewandowski, M.; Vernizzi, F. Vainshtein regime in scalar-tensor gravity: Constraints on degenerate higher-order scalar-tensor theories. *Phys. Rev. D* **2019**, *100*, 024025. [[CrossRef](#)]
75. Dima, A.; Bezares, M.; Barausse, E. Dynamical chameleon neutron stars: Stability, radial oscillations, and scalar radiation in spherical symmetry. *Phys. Rev. D* **2021**, *104*, 084017. [[CrossRef](#)]
76. Haridasu, B.S.; Karmakar, P.; De Petris, M.; Cardone, V.F.; Maoli, R. Testing generalized scalar-tensor theories of gravity with clusters of galaxies. *arXiv* **2021**, arXiv:2111.01101. [[CrossRef](#)]
77. Gandolfi, G.; Lapi, A.; Liberati, S. Self-gravitating Equilibria of Non-minimally Coupled Dark Matter Halos. *Astrophys. J.* **2021**, *910*, 76. [[CrossRef](#)]
78. Gandolfi, G.; Haridasu, B.S.; Liberati, S.; Lapi, A. Looking for Traces of Nonminimally Coupled Dark Matter in the X-COP Galaxy Clusters Sample. *Astrophys. J.* **2023**, *952*, 105. [[CrossRef](#)]
79. Zamani, S.; Salzano, V.; Bettoni, D. Gravitational lensing from clusters of galaxies to test disformal couplings theories. *Eur. Phys. J. C* **2024**, *84*, 618. [[CrossRef](#)]
80. Benetti, F.; Lapi, A.; Gandolfi, G.; Butt, M.A.; Boumechta, Y.; Haridasu, B.S.; Baccigalupi, C. Dark Matter in Fractional Gravity III: Dwarf Galaxies Kinematics. *Universe* **2023**, *9*, 478. [[CrossRef](#)]
81. Euclid Collaboration; Mellier, Y.; Abdurro'uf; Acevedo Barroso, J.A.; Achúcarro, A.; Adamek, J.; Adam, R.; Addison, G.E.; Aghanim, N.; Aguena, M.; et al. Euclid. I. Overview of the Euclid mission. *arXiv* **2024**, arXiv:2405.13491.

-
82. McElwain, M.W.; Feinberg, L.D.; Perrin, M.D.; Clampin, M.; Mountain, C.M.; Lallo, M.D.; Lajoie, C.P.; Kimble, R.A.; Bowers, C.W.; Stark, C.C.; et al. The James Webb Space Telescope Mission: Optical Telescope Element Design, Development, and Performance. *Publ. Astron. Soc. Pac.* **2023**, *135*, 058001. [[CrossRef](#)]
 83. Barret, D.; Decourchelle, A.; Fabian, A.; Guainazzi, M.; Nandra, K.; Smith, R.; den Herder, J. The Athena space X-ray observatory and the astrophysics of hot plasmat. *Astron. Nachrichten* **2020**, *341*, 224–235. [[CrossRef](#)]

Disclaimer/Publisher’s Note: The statements, opinions and data contained in all publications are solely those of the individual author(s) and contributor(s) and not of MDPI and/or the editor(s). MDPI and/or the editor(s) disclaim responsibility for any injury to people or property resulting from any ideas, methods, instructions or products referred to in the content.